Theoretical & Applied Mechanics Letters 7 (2017) 199–206

Contents lists available at ScienceDirect

Theoretical & Applied Mechanics Letters

journal homepage: www.elsevier.com/locate/taml

Letter

A chemo-mechanical model coupled with thermal effect on the hollow core–shell electrodes in lithium-ion batteries

Bin Hu [a], Zengsheng Ma [a,*], Weixin Lei [a], Youlan Zou [a], Chunsheng Lu [b]

[a] National-Provincial Laboratory of Special Function Thin Film Materials, and School of Materials Science and Engineering, Xiangtan University, Hunan 411105, China

[b] Department of Mechanical Engineering, Curtin University, Perth, WA 6845, Australia

HIGHLIGHTS

- We present a continuum model which involves thermal, chemical and mechanical behaviors.
- The electrode geometry plays an important role in diffusion kinetics of Li-ions.
- A higher local compressive stress results in a lower Li-ion concentration.

ARTICLE INFO

Article history:
Received 28 November 2016
Received in revised form 8 May 2017
Accepted 22 August 2017
Available online 14 September 2017
*This article belongs to the Solid Mechanics

Keywords:
Lithium-ion battery
Diffusion-induced stress
COMSOL
Chemo-mechanical
Electrode

ABSTRACT

Electrode is a key component to remain durability and safety of lithium-ion (Li-ion) batteries. Li-ion insertion/removal and thermal expansion mismatch may induce high stress in electrode during charging and discharging processes. In this paper, we present a continuum model based on COMSOL Multiphysics software, which involves thermal, chemical and mechanical behaviors of electrodes. The results show that, because of diffusion-induced stress and thermal mismatch, the electrode geometry plays an important role in diffusion kinetics of Li-ions. A higher local compressive stress results in a lower Li-ion concentration and thus a lower capacity when a particle is embedded another, which is in agreement with experimental observations.

Lithium-ion batteries (LIBs) have emerged as the most promising energy storage technology in recent years due to their higher energy density, lighter weight, no memory effect, and lower self-discharge rate in comparison to other rechargeable batteries [1,2]. The thermal characteristics of LIBs are intensively studied through the model analysis and experimental measurements. Especially, some coupled thermal-electrochemical models have been developed based on the electrochemical reaction and energy balance [3–5]. For example, Bernardi et al. [6] presented a general energy balance for battery systems. Chen and Evans [4,7,8] introduced two- and three-dimensional thermal models based on transient heat-transfer and heat generation equations. The convective and radiative heat transfers on surface were considered as boundary conditions, and the container of battery was incorporated to facilitate calculations. An electrochemical-thermal model, coupling a two-dimensional (2-D) thermal model with a one-dimensional (1-D) electrochemical model, was developed to examine the relationship between thermal and electrochemical behaviors [9]. These coupled models are helpful to understanding of thermal behaviors of LIBs and their design and optimization as well as thermal management during charging and discharging progress.

Furthermore, diffusion-induced stress plays an important role in the Li-ion concentration distribution [10–12]. Hao and Fang [13,14] analyzed core–shell electrode materials by introducing diffusion-induced stress. Wang et al. [15] investigated the effects of chemical stress on diffusion in a hollow cylinder.

As is well known, mechanical degradation is still a limiting factor for commercialization of high-capacity electrodes [16,17]. Volumetric swelling and shrinking in these anodes and Li-rich cathodes ranges from tens to a few hundred percent during charge and discharge cycles [18–20]. Lithiation induced volume deformation may lead to cracking and debonding of core–shell structural electrode particles. This can result in electrical disconnection that renders portions of active materials incapable of participating in Li

* Corresponding author.
E-mail address: zsma@xtu.edu.cn (Z. Ma).

http://dx.doi.org/10.1016/j.taml.2017.09.001

List of Symbols

c_l	Li-ion concentration in electrolyte, mol · m^{-3}
D_l^{eff}	effective diffusivity, m^2 · s^{-1}
F	Faraday's constant, C · mol^{-1}
i_l	current density in electrolyte, A · m^{-2}
t_+	transport number
S_a	specific surface area of electrode
j_n	charge transfer current density at the interface, A · m^{-2}
R	gas constant, J · (K · mol)$^{-1}$
T	temperature, K
f	ionic activity coefficient
i_s	current density of solid phase, A · m^{-2}
Q_s	current source
C_p	heat capacity, J · (kg · K)$^{-1}$
k	thermal conductivity, W · (m^{-2} · K^{-1})
Q	heat generation rate per unit volume
h	convective heat transfer coefficient, W · (m^{-2} · K^{-1})
T_{amb}	ambient temperature, K
a	initial inner radius of a hollow particle, μm
b	initial outer radius of a hollow particle, μm
d	initial outer radius of a shell, μm
J	diffusion flux
D_{ref}	diffusivity without stress, m^2 · s^{-1}
E_{act}	activation energy, J · mol^{-1}
E	Young's modulus, GPa
v	Poisson's ratio
L_N	Negative electrode length, μm
L_P	Positive electrode length, μm
L_S	Separator length, μm
L_{NCC}	Negative current collector length, μm
L_{PCC}	Positive current collector length, μm
R_N	Negative active particle radius, μm
R_P	Positive active particle radius, μm

Greek

ε	porosity
σ_l^{eff}	effective ionic conductivity, S · m^{-1}
Φ_l	ionic potential, V
σ_s	electronic conductivity, S · m^{-1}
ϕ_s	electronic potential,V
ρ	density, kg · m^{-3}
σ_h	hydrostatic stress, GPa
Ω	partial molar volume, m^3 · mol^{-1}
γ	positive dimensionless coefficient
ε_{ij}	strain components
σ_{ij}	stress components, GPa
Δc	Li-ion concentration change
δ_{ij}	Kronecker delta
α	coefficient of thermal expansion, K^{-1}
ΔT	temperature change
σ_r	radial stress, GPa
σ_θ	hoop stress, GPa

storage. Meanwhile, mechanical stress significantly derives from thermodynamics and kinetics of lithiation reactions, ion diffusion, and phase transition [21–25].

Recently, $LiMn_2O_4$ has been generally used as the positive electrode material in commercial Li-ion batteries. Christensen and Newman [26] developed a fully-coupled diffusion-mechanics model to simulate stress generation and predict fracture in spherical $Li_yMn_2O_4$ particles. Zhang et al. [27,28] studied intercalation-induced stress and heat generation in Mn_2O_4 particles based on Butler–Volmer surface reaction kinetics.

In this paper, by using COMSOL Multiphysics, we present a coupling mechanical model with thermal effect and electrochemistry to investigate the distribution of solute concentration and diffusion-induced stress in a hollow core–shell electrode.

The 1-D battery model considers an electrochemical system that consists of a negative electrode, a separator, and a positive electrode. The electrodes and separator are porous and saturated with liquid electrolyte. The porous solid together with electrolyte is modeled as a homogenized composite medium. The volume fraction of electrolyte equals the porosity. The contribution of electrolyte in Li-ion transport is considered by introducing a porosity parameter in the governing equation.

In the COMSOL model, Li-ion in electrolyte is transported through diffusion and migration. The Li-ion transport balance equation can be described by [29]

$$\varepsilon \frac{\partial c_l}{\partial t} = \nabla \cdot \left(D_l^{eff} \nabla c_l - \frac{i_l}{F} t_+ \right) + S_a j_n (1 - t_+), \tag{1}$$

where ε is porosity, c_l is the Li-ion concentration, D_l^{eff} is effective diffusivity and $D_l^{eff} = \varepsilon^{1.5} D_l$ with D_l the diffusivity, $F = 96487\text{C mol}^{-1}$ is Faraday's constant, i_l is the current density, t_+ is the transport number representing the percentage of current carried by Li-ion, S_a is the specific surface area, and j_n is the charge transfer current density at interface, which is defined by

$$j_n = \frac{\nabla \cdot i_l}{S_a F}. \tag{2}$$

In Eq. (1), the gradient of Li-ion concentration can be determined by Li-ion diffusion (the 1st term), Li-ion migration in an electrical field (the 2nd term), and the concentration change between electrolyte and active particles (the 3rd term).

Based on the ionic charge balance, we have

$$\nabla \cdot \left[-\sigma_l^{eff} \nabla \phi_l + \frac{2\sigma_l^{eff} RT}{F} \left(1 + \frac{\partial \ln f}{\partial \ln c_l} \right) (1 - t_+) \nabla (\ln c_l) \right] = S_a j_n, \tag{3}$$

where $\sigma_l^{eff} = \varepsilon^{1.5} \sigma_l$ is the effective ionic conductivity with σ_l the ionic conductivity in electrolyte, Φ_l is the ionic potential, R is the gas constant, T is temperature, and f is the ionic activity coefficient. Here, the 1st term is equivalent to that of a solid conductor, and the 2nd term accounts for the effect of Li-ion concentration on the ionic current.

In the solid phase of porous electrode, the Li-ion transport balance equation is given by

$$\frac{\partial c_s}{\partial t} = \nabla \cdot (D_s \nabla c_s). \tag{4}$$

The charge balance obeys Ohm's law, that is

$$\nabla \cdot i_s = Q_s, \tag{5}$$

where i_s is the current density of solid phase and Q_s denotes the current source. Here,i_s can be described as

$$i_s = -\sigma_s \nabla \phi_s, \tag{6}$$

where σ_s and ϕ_s are electronic conductivity and electronic potential, respectively.

In the model, positive and negative electrodes are $Li_yMn_2O_4$ and Li_xC_6, respectively. The electrolyte is $LiPF_6$ dissolved in a mixture of 3:7 EC/EMC. Their main geometry parameters are given in Table 1.

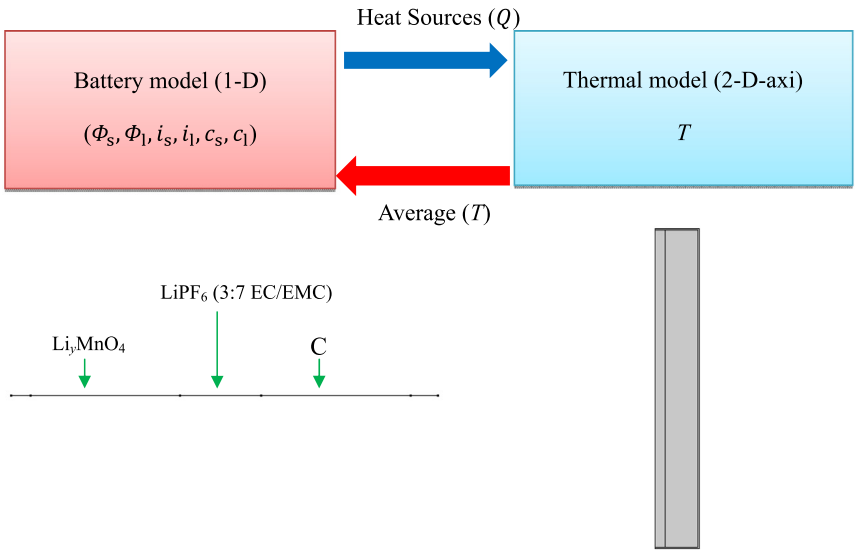

Fig. 1. The coupled relationship.

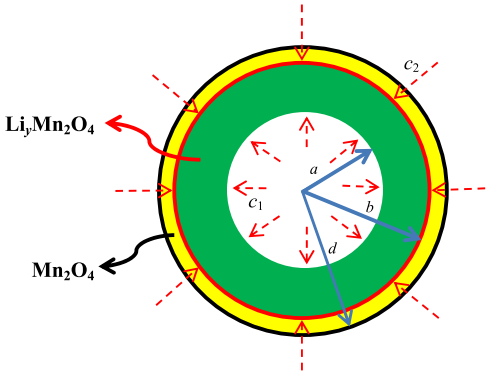

Fig. 2. Sketch of a core–shell structure.

Table 1
Dimensions of components in the 1-D battery model.

Parameter	Value
R_N (μm)	2.5
R_P (μm)	1.7
L_N (μm)	50
L_P (μm)	50
L_S (μm)	30
L_{NCC} (μm)	10
L_{PCC} (μm)	10

All other parameters in the model were kept the same as those in the original 1-D battery model in COMSOL 5.0.

A 2-D electrode thermal model is formulated based on the thermal energy balance in a representative elementary volume of LIBs. The transient heat transfer can be represented as

$$\rho C_p \frac{\partial T}{\partial t} = \nabla \cdot (k \nabla T) + Q, \tag{7}$$

where ρ, C_p, k and Q are the density, heat capacity, thermal conductivity and heat-generation rate per unit volume, respectively.

The heat generation source Q is divided into three parts: reaction heat Q_{rea}, activation polarization heat Q_{act}, and ohmic heat Q_{ohm}, that is

$$Q = Q_{rea} + Q_{act} + Q_{ohm}, \tag{8}$$

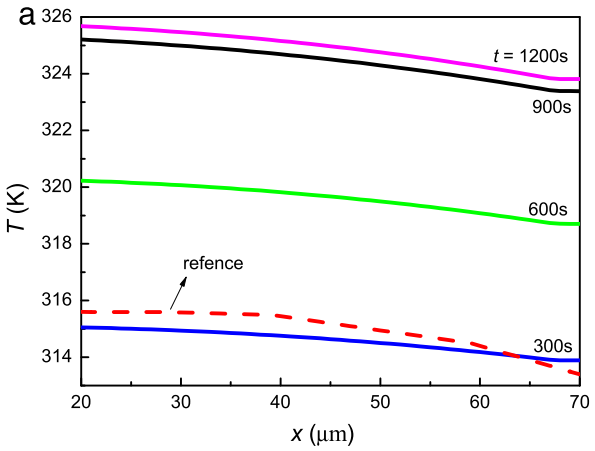

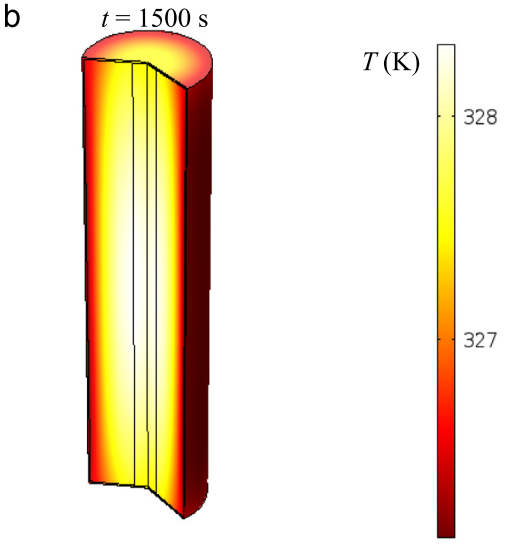

Fig. 3. Distributions of temperature at 300, 600, 900, and 1200 s, and (b) distribution of temperature in electrode.

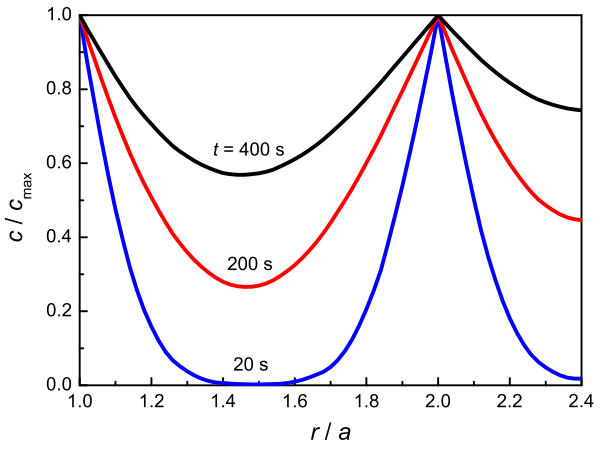

Fig. 4. Distributions of concentration at 20, 200, and 400 s along the radial direction.

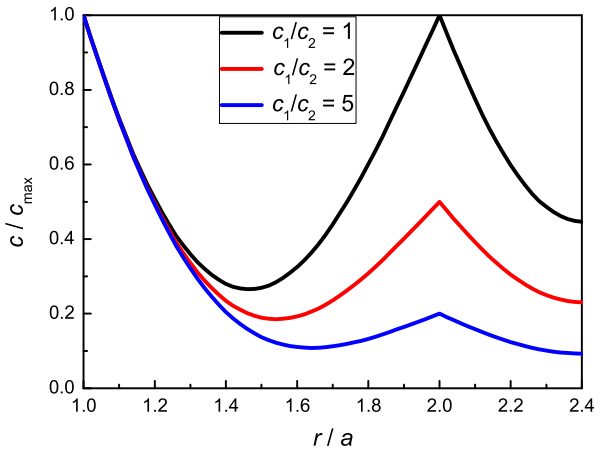

Fig. 5. Distributions of concentration with different concentration ratios along the radial direction.

$$Q_{\mathrm{rea}} = S_{\mathrm{a}} j_{\mathrm{n}} T \frac{\partial U_{\mathrm{eq}}}{\partial T}, \tag{9}$$

with U_{eq} is the open circuit potential of the electrode,

$$Q_{\mathrm{act}} = S_{\mathrm{a}} j_{\mathrm{n}} \eta, \tag{10}$$

with the overpotential η defined as $\eta = \phi_{\mathrm{l}} - \phi_{\mathrm{s}} - U_{\mathrm{eq}}$, and

$$Q_{\mathrm{ohm}} = -i_{\mathrm{s}} \nabla \phi_{\mathrm{s}} - i_{\mathrm{l}} \nabla \phi_{\mathrm{l}}. \tag{11}$$

On the boundary, the convective heat transfer can be expressed as

$$-k \frac{\partial T}{\partial n} = h\,(T - T_{\mathrm{amb}})\,, \tag{12}$$

where h, T and T_{amb} denote the convective heat transfer coefficient, surface temperature and ambient temperature, respectively.

Because the cell temperature is only dependent on time, side reactions inside the battery can be omitted. The effect of kinetic and transport parameters on temperature can be described by

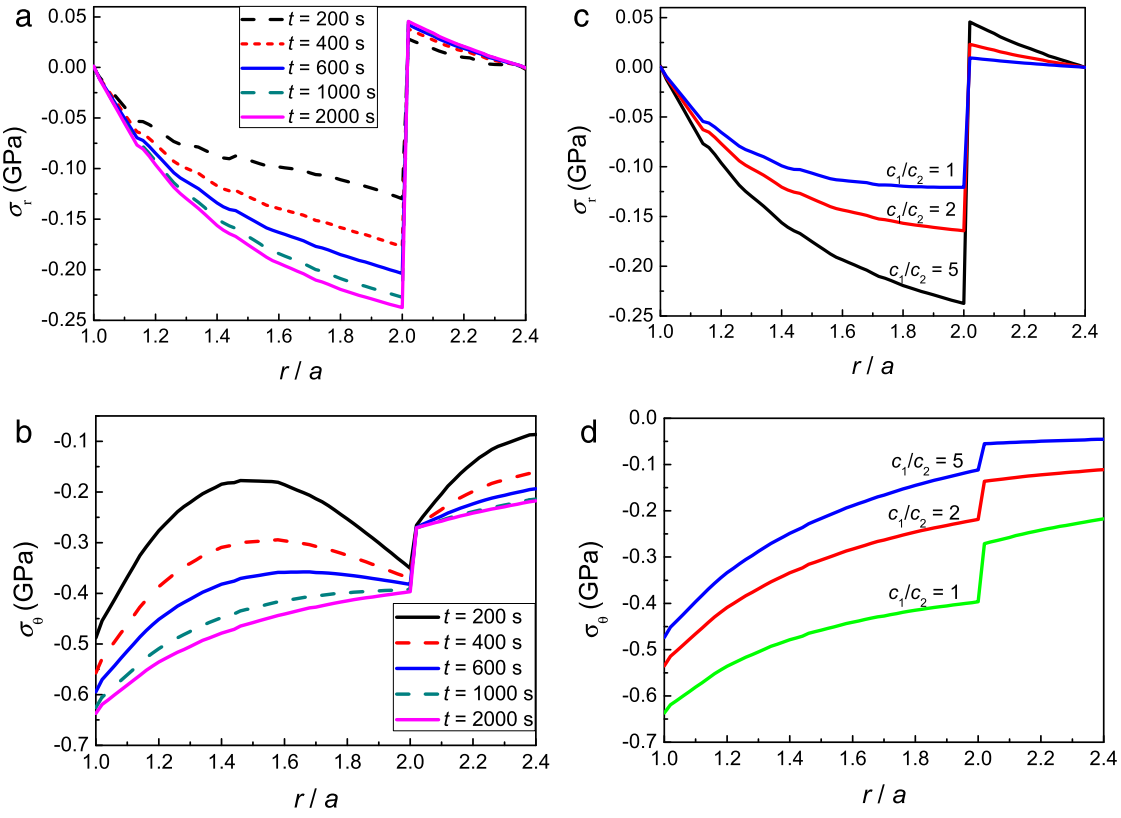

Fig. 6. Distributions of sphere radial and hoop stresses under different times and concentration ratios along the radial direction.

Table 2
Material constants of $Li_yMn_2O_4$.

Parameters	Value
Ω ($m^3 \cdot mol^{-1}$)	3.50×10^{-6}
α (K^{-1})	8.62×10^{-6}
c_{max} ($mol \cdot m^{-3}$)	2.29×10^4
D_{ref} ($m^2 \cdot s^{-1}$)	7.08×10^{-15}
E_{act} ($J \cdot mol^{-1}$)	2.00×10^4
E (GPa)	10
ν	0.30
ρ ($kg \cdot m^{-3}$)	4202
C_p ($J\,(kg \cdot K)^{-1}$)	672
K ($W\,(m \cdot K)^{-1}$)	6.20

Table 3
Material constants of Mn_2O_4.

Parameters	Value
D ($m^2 \cdot s^{-1}$)	7.08×10^{-15}
E (GPa)	10
ν	0.30
Ω ($m^3 \cdot mol^{-1}$)	3.49×10^{-6}
c_{max} ($mol \cdot m^{-3}$)	2.29×10^4

Arrhenius type expression [30,31], that is

$$P = P_{ref} \exp\left[\frac{E_{act}}{R}\left(\frac{1}{T_{ref}} - \frac{1}{T}\right)\right]. \quad P = D_s, D_l, i_s, i_l, U_{eq} \tag{13}$$

Other parameters (e.g., σ_s, σ_l, Φ_s, Φ_l, ρ, C_p, k, h) are taken to be temperature-independent constants.

The coupling relationship between the battery and thermal models is depicted in Fig. 1. The battery model generates the heat source profile in solid and electrolyte phase of electrodes to simulate the electrode temperature distribution.

A core–shell structure subjected to variation of temperature and concentration is pre-existent in a hollow spherical electrode, as shown in Fig. 2. The inner core is $Li_yMn_2O_4$, and the outer shell is Mn_2O_4. Their material properties used are listed in Tables 2 and 3 for $Li_yMn_2O_4$ [5,27,32–34] and Mn_2O_4 [35], respectively.

The driving force μ of Li-ion diffusion can be obtained by the gradient of characteristic potential comprising the chemical and elastic energy of the system, which can be represented as

$$\mu = \mu_0 + RT \ln(c) - \Omega\sigma_h, \tag{14}$$

where μ_0 is a constant, R is the gas constant, T is absolute temperature, σ_h is hydrostatic stress from the elastic field, and Ω is the partial molar volume.

The diffusion flux J is given by [27]

$$J = D\left(-\nabla c + \frac{\Omega c}{RT}\nabla\sigma_h\right), \tag{15}$$

where the temperature and stress dependence on the diffusion coefficient D is calculated by

$$D = D_{ref} \times \exp\left[\frac{E_{act}}{R}\left(\frac{1}{T_{ref}} - \frac{1}{T}\right)\right] \times \exp\left(\frac{\gamma\Omega\sigma_h}{RT}\right), \tag{16}$$

where D_{ref} is the diffusivity without stress, E_{act} is activation energy and γ is a positive dimensionless coefficient representing the linear dependency of diffusion activation energy on hydrostatic stress. The constant $T_{ref} = 298$ K is chosen for the core–shell system. To remain the numerical stability, the maximum D is limited to $10^4 \times D_{ref}$ [36].

In Eq. (15), the 1st term on the right-hand side accounts for the effect of concentration gradient, and the 2nd term represents the effect of stress gradient. Submitting Eq. (15) into the mass conservation equation, $\frac{\partial c}{\partial t} + \nabla \cdot J = 0$, we have

$$\frac{\partial c}{\partial t} - \nabla \cdot \left[D\left(\nabla c - \frac{\Omega c}{RT}\nabla\sigma_h\right)\right] = 0, \tag{17}$$

which governs the evolution of Li-ion concentration.

Considering various solute concentrations of hollow core–shell electrode during charging and discharging, the boundary conditions (see Fig. 2) can be written as

$$c\,(t=0) = c_1, \quad \text{at } r = a,$$

$$c\,(t=0) = c_2, \quad \text{at } r = b,$$

$$c\,(t=0) = c_0, \quad \text{at } a < r < b \text{ and } b < r < d. \tag{18}$$

In this study, the electrode material is assumed to be isotropic, homogeneous and linear elastic under plane-strain and quasi-static deformation. The stress field can be solved by

$$\nabla \cdot \boldsymbol{\sigma} = 0. \tag{19}$$

The strain–displacement relations can be expressed by

$$\varepsilon_{ij} = \frac{1}{E}\left[(1+\nu)\sigma_{ij} - \nu\sigma_{kk}\delta_{ij}\right] + \frac{\Omega}{3}\Delta c\delta_{ij} + \alpha\,\Delta T\delta_{ij}, \tag{20}$$

where ε_{ij} and σ_{ij} are strain and stress components, respectively. E is Young's modulus, ν is Poisson's ratio, Δc is the Li-ion concentration change, δ_{ij} is the Kronecker delta, α is the coefficient of thermal expansion, and ΔT is the temperature change. Here, the variation of elastic constants with temperature and Li-ion concentration is ignored. The boundary condition is $u\,(r = b) = 0$.

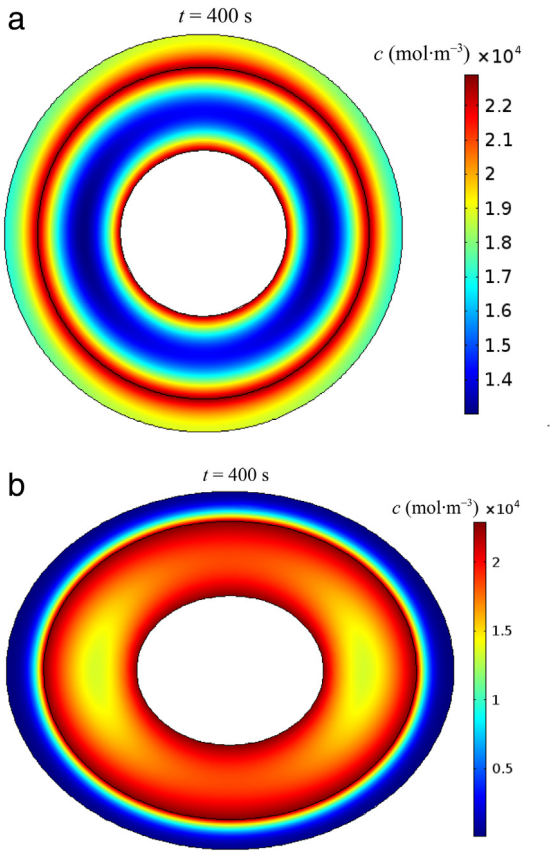

Fig. 7. Distributions of concentration in (a) sphere and (b) ellipsoid electrodes at 400 s.

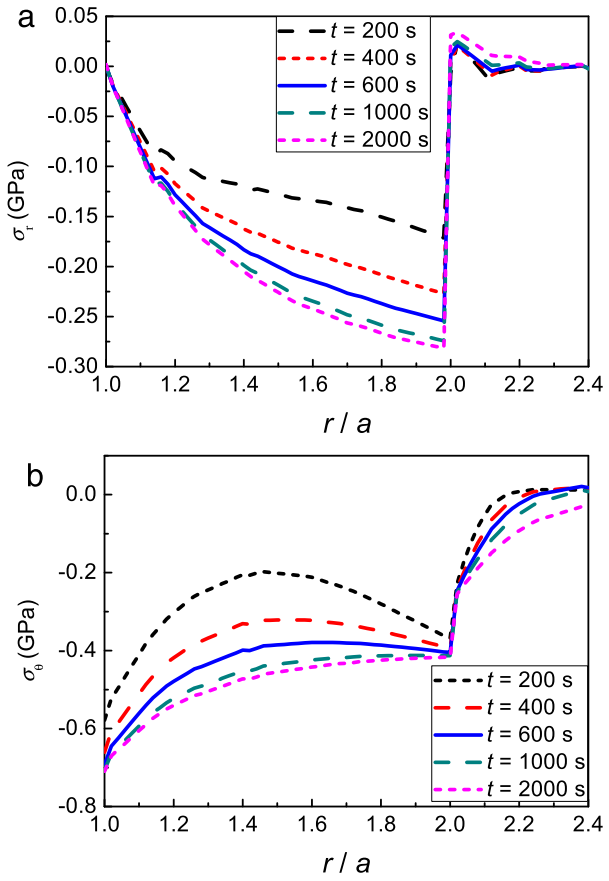

Fig. 8. Distributions of (a) radial and (b) hoop stresses in ellipsoid under different times along the radial direction.

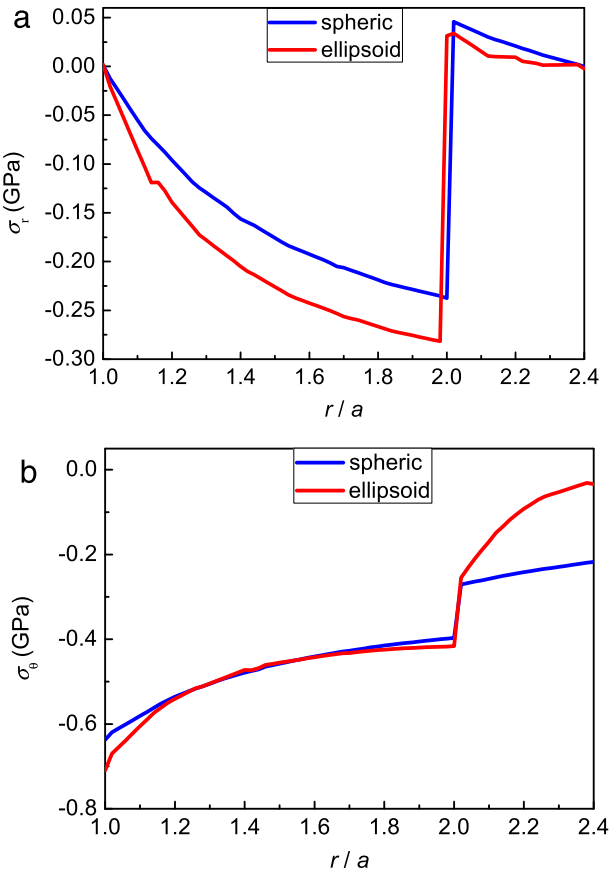

Fig. 9. Distributions of (a) radial and (b) hoop stresses along the radial direction.

The temperature distribution is solved by using COMSOL Multiphysics. It is shown that the electrode operating temperature between the center and surface ranges from 314 to 326 K with $h = 20\,\mathrm{W}\cdot(\mathrm{m}^{-2}\cdot\mathrm{K}^{-1})$ (see Fig. 3(a)). The temperature distribution is not symmetrical, viz, the maximum temperature locates at the center of battery and the side temperature is below the maximum temperature, as shown in Fig. 3(b), which agrees with experiment measurements [37].

Figure 4 shows the concentration distribution in the case of $b/a = 2$ and $c_1/c_2 = 1$ between the core–shell spherical electrode under different times. The higher concentrations appear on the core inner and outer surfaces, resulting in Li-ion diffusion toward the middle core and shell. With increasing diffusion time, Li-ions diffuse from high to low concentrations. Hence, the Li-ion concentration in hollow spherical core–shell structure finally approaches a steady state of c_1. In Fig. 5, the concentration difference increases with increasing the concentration ratio c_1/c_2 between the core inner and outer surfaces at $t = 1200$ s. With lithiation going, the core–shell interface of electrode experiences larger concentration difference, which may cause large tensile stress, causing crack nucleation in the active area of core–shell interface and shell debonding. Thus, we can control the lithiation rate to improve electrode cycle performance.

As illustrated in Fig. 6, the initial stress evolution plays an important role in the mechanical properties of electrodes [38,39]. For hollow spherical core–shell electrode with high concentration, electrochemical decay of LIBs may occur since high stress in electrode can easily cause debonding of shell electrode. With the increase of diffusion time, the core compressive stress increases along the radial direction. Higher compressive stress results in lower Li-ion concentration and diffusion rate. However, on the core–shell interface, the radial stress is transferred from compression to tension; this may cause shell debonding. Although a brittle material is sensitive to tensile stress, a large compressive stress may also cause failure [10,40] because the core compressive stress is much higher than the maximum tensile stress on the core–shell interface. Figure 6(c) and (d) show radial and hoop stresses under different concentration ratios. With increasing the concentration ratio, the radial stress increases, while the hoop stress decreases along the radial direction, which is in agreement with the concentration change.

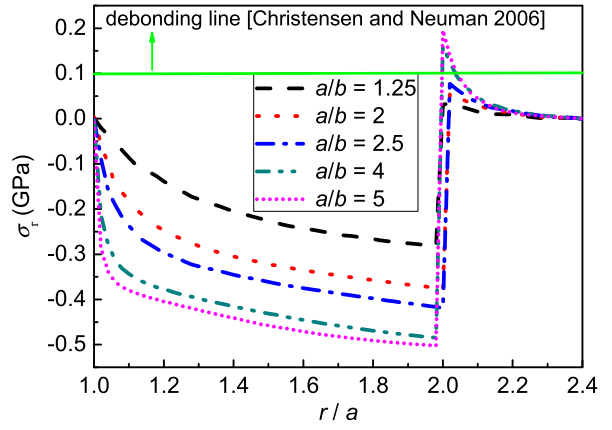

Fig. 10. Distributions of radial stress with different radius ratio a/b along the radial direction.

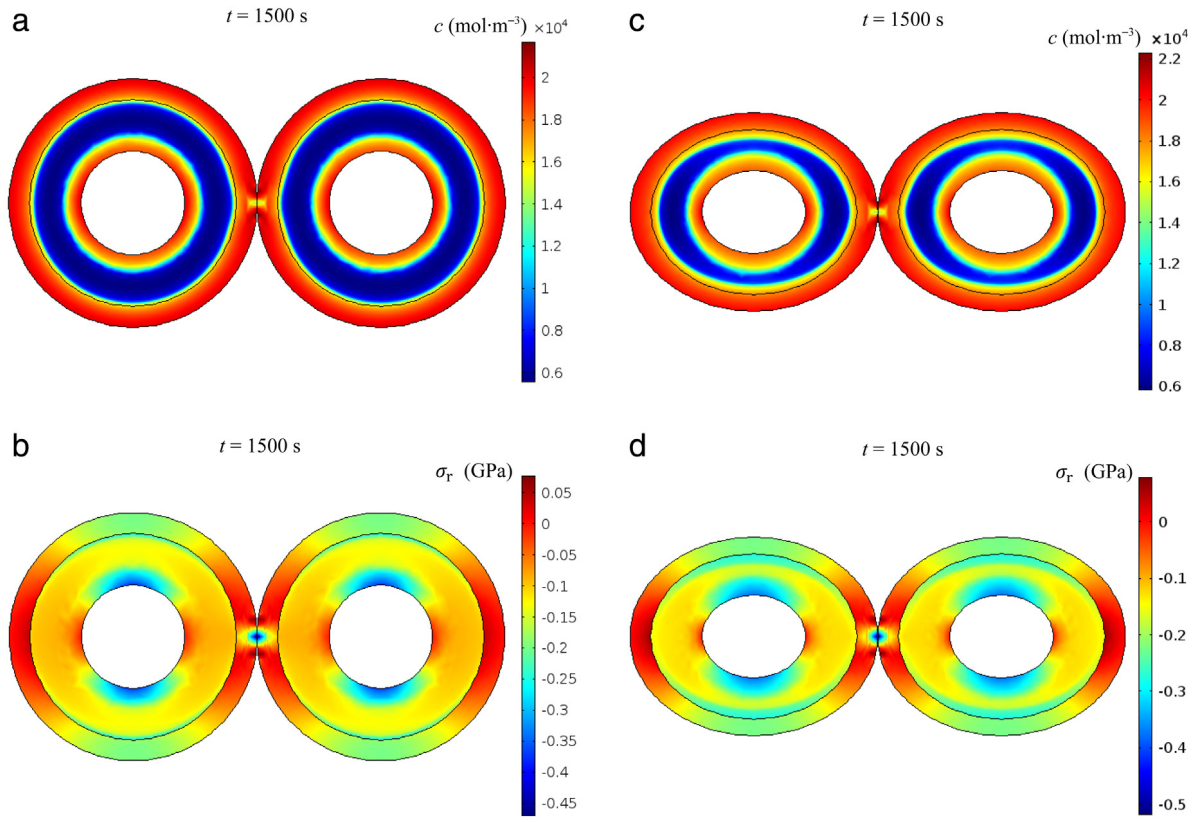

Fig. 11. Two embedded particle electrodes at 1500 s, where (a) and (b) are distributions of concentration and stress in sphere electrodes, and (c) and (d) are distributions of concentration and stress in ellipsoid electrodes.

Figure 7 represents the concentration distribution of spherical and ellipsoidal electrode at 400 s. Obviously, the concentration distribution in spherical electrode is uniform, while it is nonuniform in ellipsoidal electrode. Such inhomogeneity is dominated by geometric effects. Figure 8 shows ellipsoidal radial and hoop stresses under different times, with the radial stress is along the radial direction ($\theta = 0°$). It is seen that the ellipsoidal stress has the same trend with that of spherical electrode along the radial direction. With increasing diffusion time, the core compressive stress increases along the radial direction. On the core–shell interface, however, the radial stress is transferred from compression to tension. As shown in Fig. 9, radial and hoop stresses in ellipsoid are higher than that in sphere electrode, with the radial stress is along the radial direction ($\theta = 0°$). Therefore, ellipsoid is easier to fracture than sphere electrode in the same condition. Due to Li-ion intercalation and thermal mismatch, the geometry of electrodes has a significant influence on diffusion of electrodes. With increasing the radius ratio a/b, radial tensile stress along the radial direction ($\theta = 0°$) increases quickly. According to Christensen and Newman [26], tensile strength of the Li manganese particle is close to 100 MPa. With increasing the radius ratio a/b, the core–shell interfacial may suffer debonding along the radial direction ($\theta = 0°$) (see Fig. 10). Thus, an optimum electrode structure and effective Li storage strategy can be realized by controlling the electrode geometry.

As shown in Fig. 11, the effect of mechanical interaction on the Li-ion distribution becomes dominant and Li-ion profiles are highly inhomogeneous. A highly asymmetric stress field develops in the contact zone, which consequently decreases Li-ion concentrations. The larger compressive stress occurs in the particle contact zone. Insertion of Li-ions is blocked by local high compressive stress, which significantly reduces the effective capacity of particles. This confinement generates a large local compressive stress and drastically alters the profile of Li chemical potential, which is in agreement with experiments [41].

We developed a finite element model based on a theoretical framework coupling thermal, electrochemistry and stress in electrodes of LIBs. This model enables us to model the coupling behavior of different geometric electrodes and to explore lithiation kinetics and evolution of mechanical stress. The Li-ion profiles and stress distributions in geometric electrodes are significantly different from each other. It is shown that the concentration and stress distribution in core–shell electrodes can be optimally designed by controlling the concentration ratio, geometry, and pattern of active particles. This study highlights the strong coupling between the electrochemistry of thermal, diffuse and mechanical stress in core–shell electrodes and provides important insight on design of resilient LIB electrodes.

Acknowledgment

This work has been supported by the National Natural Science Foundation of China (11702234 and 11602213).

References

[1] K. Chen, S. Song, F. Liu, et al., Structural design of graphene for use in electrochemical energy storage devices, Chem. Soc. Rev. 44 (2015) 6230–6257.
[2] M. Plaimer, C. Breitfuß, W. Sinz, et al., Evaluating the trade-off between mechanical and electrochemical performance of separators for lithium-ion batteries: methodology and application, J. Power Sources 306 (2016) 702–710.
[3] Y. Chen, J.W. Evans, Thermal analysis of lithium polymer electrolyte batteries by a two dimensional model—thermal behaviour and design optimization, Electrochim. Acta 39 (1994) 517–526.
[4] Y. Chen, J.W. Evans, Thermal analysis of lithium-ion batteries, J. Electrochem. Soc. 143 (1996) 2708–2712.

[5] M. Doyle, J. Newman, A.S. Gozdz, et al., Comparison of modeling predictions with experimental data from plastic lithium ion cells, J. Electrochem. Soc. (1996) 1890–1903.
[6] D. Bernardi, E. Pawlikowski, J. Newman, A general energy balance for battery systems, J. Electrochem. Soc. 132 (1985) 5–12.
[7] Y. Chen, J.W. Evans, Heat transfer phenomena in lithium/polymer-electrolyte batteries for electric vehicle application, J. Electrochem. Soc. 140 (1993) 1833–1838.
[8] Y. Chen, J.W. Evans, Three-dimensional thermal modeling of lithium-polymer batteries under galvanostatic discharge and dynamic power profile, J. Electrochem. Soc. 141 (1994) 2947–2955.
[9] L. Song, J.W. Evans, Electrochemical-thermal model of lithium polymer batteries, J. Electrochem. Soc. 147 (2000) 2086–2095.
[10] Z. Ma, Z. Xie, Y. Wang, et al., Failure modes of hollow core–shell structural active materials during the lithiation-delithiation process, J. Power Sources 290 (2015) 114–122.
[11] Y. Wang, Y. Pu, Z. Ma, et al., Interfacial adhesion energy of lithium-ion battery electrodes, Extreme Mech. Lett. 9 (2016) 226–236.
[12] Z. Ma, T. Li, Y. Huang, et al., Critical silicon-anode size for averting lithiation-induced mechanical failure of lithium-ion batteries, RSC Adv. 3 (2013) 7398–7402.
[13] F. Hao, D. Fang, Tailoring diffusion-induced stresses of core–shell nanotube electrodes in lithium-ion batteries, J. Appl. Phys. 113 (2013) 013507.
[14] F. Hao, D. Fang, Diffusion-induced stresses of spherical core–shell electrodes in lithium-ion batteries: the effects of the shell and surface/interface stress, J. Electrochem. Soc. 160 (2013) A595–A600.
[15] W. Wang, S. Lee, J. Chen, Effect of chemical stress on diffusion in a hollow cylinder, J. Appl. Phys. 91 (2002) 9584–9590.
[16] Z. Ma, H. Wu, Y. Wang, et al., An electrochemical-irradiated plasticity model for metallic electrodes in lithium-ion batteries, Int. J. Plast. 88 (2017) 188–203.
[17] Z. Ma, Z. Xie, Y. Wang, et al., Softening by electrochemical reaction-induced dislocations in lithium-ion batteries, Scr. Mater. 127 (2017) 33–36.
[18] L. Beaulieu, K. Eberman, R. Turner, et al., Colossal reversible volume changes in lithium alloys, Electrochem. Solid-State Lett. 4 (2001) A137–A140.
[19] H. Kim, J.T. Lee, A. Magasinski, et al., In situ TEM observation of electrochemical lithiation of sulfur confined within inner cylindrical pores of carbon nanotubes, Adv. Energy Mater. 5 (2015).
[20] J. Li, B.L. Armstrong, J. Kiggans, et al., Lithium ion cell performance enhancement using aqueous $LiFePO_4$ cathode dispersions and polyethyleneimine dispersant, J. Electrochem. Soc. 160 (2013) A201–A206.
[21] K. Zhao, M. Pharr, Q. Wan, et al., Concurrent reaction and plasticity during initial lithiation of crystalline silicon in lithium-ion batteries, J. Electrochem. Soc. 159 (2012) A238–A243.
[22] M.T. McDowell, S.W. Lee, C. Wang, et al., Studying the kinetics of crystalline silicon nanoparticle lithiation with in situ transmission electron microscopy, Adv. Mater. 24 (2012) 6034–6041.
[23] H. Yang, W. Liang, X. Guo, et al., Strong kinetics-stress coupling in lithiation of Si and Ge anodes, Extreme Mech. Lett. 2 (2015) 1–6.
[24] G. Sandu, L. Brassart, J.-F. Gohy, et al., Surface coating mediated swelling and fracture of silicon nanowires during lithiation, ACS Nano 8 (2014) 9427–9436.
[25] A. Mukhopadhyay, B.W. Sheldon, Deformation and stress in electrode materials for Li-ion batteries, Prog. Mater. Sci. 63 (2014) 58–116.
[26] J. Christensen, J. Newman, A mathematical model of stress generation and fracture in lithium manganese oxide, J. Electrochem. Soc. 153 (2006) A1019–A1030.
[27] X. Zhang, W. Shyy, A.M. Sastry, Numerical simulation of intercalation-induced stress in Li-ion battery electrode particles, J. Electrochem. Soc. 154 (2007) A910–A916.
[28] X. Zhang, A.M. Sastry, W. Shyy, Intercalation-induced stress and heat generation within single lithium-ion battery cathode particles, J. Electrochem. Soc. 155 (2008) A542–A552.
[29] X. Xiao, W. Wu, X. Huang, A multi-scale approach for the stress analysis of polymeric separators in a lithium-ion battery, J. Power Sources 195 (2010) 7649–7660.
[30] M. Guo, G. Sikha, R.E. White, Single-particle model for a lithium-ion cell: thermal behavior, J. Electrochem. Soc. 158 (2011) A122–A132.
[31] P.M. Gomadam, J.W. Weidner, R.A. Dougal, et al., Mathematical modeling of lithium-ion and nickel battery systems, J. Power Sources 110 (2002) 267–284.
[32] J.F. Shackelford, W. Alexande, Materials Science and Engineering Handbook, third ed., CRC Press, 2001.
[33] V. Srinivasan, C.Y. Wang, Analysis of electrochemical and thermal behavior of Li-ion cells, J. Electrochem. Soc. 150 (2003) A98–A104.
[34] W. Wu, X. Xiao, X. Huang, The effect of battery design parameters on heat generation and utilization in a Li-ion cell, Electrochim. Acta 83 (2012) 227–240.
[35] W. Zhou, Effects of external mechanical loading on stress generation during lithiation in Li-ion battery electrodes, Electrochim. Acta 185 (2015) 28–33.
[36] S. Huang, F. Fan, J. Li, et al., Stress generation during lithiation of high-capacity electrode particles in lithium ion batteries, Acta Mater. 61 (2013) 4354–4364.
[37] L.O. ValØen, J.N. Reimers, Transport properties of $LiPF_6$-based Li-ion battery electrolytes, J. Electrochem. Soc. 152 (2005) A882–A891.
[38] Y.-T. Cheng, M.W. Verbrugge, Evolution of stress within a spherical insertion electrode particle under potentiostatic and galvanostatic operation, J. Power Sources 190 (2009) 453–460.
[39] J. Zhu, K. Zeng, L. Lu, Cycling effects on surface morphology, nanomechanical and interfacial reliability of $LiMn_2O_4$ cathode in thin film lithium ion batteries, Electrochim. Acta 68 (2012) 52–59.
[40] J. Park, W. Lu, A.M. Sastry, Numerical Simulation of Stress Evolution in lithium manganese dioxide particles due to coupled phase transition and intercalation, J. Electrochem. Soc. 158 (2011) A201–A206.
[41] R. Xu, K. Zhao, Mechanical interactions regulated kinetics and morphology of composite electrodes in Li-ion batteries, Extreme Mech. Lett. 8 (2016) 13–21.